Microsystem Technologies (2023) 29:311–320
https://doi.org/10.1007/s00542-023-05427-8

TECHNICAL PAPER

# RF MEMS variable attenuators with improved dB-linearity

Dooyoung Hah[1]

Received: 2 May 2022 / Accepted: 7 February 2023 / Published online: 22 February 2023


## Abstract

A variable attenuator is one of the essential components in radio frequency (RF) systems, such as automatic gain control amplifiers and full-duplex systems. Variable attenuators based on microelectromechanical systems (MEMS) technology have several advantages over the semiconductor counterparts, including low power consumption and suppressed harmonics. Attenuation can be realized by disruption of signal propagation, which is induced by moving electrodes placed next to a signal line. In this work, the effect of the moving electrodes on the RF characteristics of the variable attenuators is studied via numerical simulation. It is observed that 10 μm of moving electrode displacement can result in 18 dB of attenuation dynamic range at 20 GHz. The similar type of RF MEMS variable attenuators reported previously showed substantial nonlinearity in attenuation-voltage characteristics, which becomes a serious drawback for applications where high-precision attenuation management is required. The main objective of the current study is, therefore, to achieve high dB-linearity, by employing shaped-finger comb-drive actuators in the moving electrode displacement control. In addition, a nonlinear relationship between force and displacement in a clamped-clamped beam spring is taken into account for more accurate device modelling. Through finite element analysis, it is shown that an improvement by a factor of twelve can be obtained in dB-linearity by using a single-comb shaped-finger actuator, compared to standard straight-finger comb-drives. The study also shows that the dB-linearity can be further (2.2 times additionally) improved by utilizing dual-comb shaped-finger actuators.

**List of symbols**

| | |
|---|---|
| $A$ | Attenuation, equals to $-S_{21}$ |
| $C_{bias}$ | Unit 2-D capacitance, bias comb |
| $c_{dblin}$ | Coefficient of dB-linearity |
| $C_{DRIVE}$ | Unit 3-D capacitance, drive comb |
| $C_{drive}$ | Unit 2-D capacitance, drive comb |
| $d_{bias}$ | Finger gap profile, bias comb |
| $d_{drive}$ | Finger gap profile, drive comb |
| $E$ | Young's modulus |
| $F_{elec}$ | Electrostatic force |
| $F_{mech}$ | Mechanical restoring force |
| $g_{me}$ | Gap between a moving electrode and a signal line |
| $k_1$ | Spring constant, linear term |
| $k_3$ | Spring constant, cubic term |
| $l_{ol}$ | As-fabricated overlap length between fingers |
| $S_{11}$ | Reflected power at port 1, return loss |
| $S_{21}$ | Power transferred from port 1 to port 2, insertion loss |
| $u$ | Distance from the moving finger tip, drive comb |
| $V$ | Applied voltage, drive comb |
| $v$ | Distance from the moving finger tip, bias comb |
| $V_{bias}$ | Applied bias voltage, bias comb |
| $x$ | Beam center (moving electrode) displacement |
| $x_i$ | Excluded zone length |
| $x_{fex}$ | Far-side extension length |
| $x_{max}$ | Maximum displacement range |
| $x_{nex}$ | Near-side extension length |

## 1 Introduction

In radio frequency (RF) systems, a variable attenuator is one of the widely used components. A representative example is found in an automatic gain control (AGC) amplifier. AGC amplifiers are used in receivers to broaden the input signal dynamic range in various RF systems, such as mm-wave mobile backhaul transceivers (Destino et al 2017), radiometry systems used for electron cyclotron emission measurements (Kumar et al 2019), and so on. AGC amplifiers can be implemented by using either a

✉ Dooyoung Hah
dooyoung.hah@agu.edu.tr

[1] Department of Electrical & Electronics Engineering, Abdullah Gül University, Erkilet Blv, Kayseri 38080, Turkey

variable gain amplifier or a variable attenuator. In some RF transceivers, variable attenuators are employed both at the transmitter and at the receiver to compensate the signal strength variation and temperature-change-induced gain variation (Levinger et al 2016). Variable attenuators are also used for gain control in phased-array radar systems (Gao et al 2021; Zhao et al 2021). In full duplex systems, variable attenuators can be incorporated to improve inter-port isolation, where it is called an RF canceller (Kolodziej et al 2016; Nawaz and Tekin 2016).

Conventional RF variable attenuators have been implemented by using semiconductor device technologies such as RF complementary metal-oxide-semiconductor (CMOS) field-effect transistors (Huang et al 2011), monolithic microwave integrated circuits (MMICs) (Wang et al 2017) and p-i-n diodes (Sun et al 2005). Being active components, however, these semiconductor-device-based variable attenuators inherently suffer from high power consumption and incurrence of harmonics, which make them less attractive for applications that require high linearity performances. In the place of active semiconductor devices, passive components such as microelectromechanical systems (MEMS) devices can become good alternatives, which consume minimal standing power and do not incur harmonics. A range of RF MEMS devices have been reported so far, including switches (Saleh et al 2022; Sravani et al 2022), variable capacitors (Sharaf et al 2022; Ture Savadkoohi and Margesin 2022), filters (Habbachi and Besbes 2022), resonators (Workie et al 2022), and inductors (Chang and Sivoththaman 2006).

Recently, variable attenuators have been added to this list of RF MEMS devices. The device reported by Khaira et al (2019) incorporates moving electrodes within coplanar waveguides (CPWs). The moving electrodes were controlled by Chevron actuators, and 15 dB of attenuation range was obtained at 60 GHz. Iannacci and Tagliapietra (2022) reported monolithic step attenuators, which employ five cantilever-based switches to realize fifteen different levels of attenuation.

There is another kind of linearity desired in variable attenuators apart from the one related to harmonics. This linearity is between the control voltage and the attenuation in dB, which is often called dB-linearity. High dB-linearity enables precise attenuation control throughout the entire dynamic range, and hence is required in some systems and desired in others. It can also prevent system control instability that is caused by high nonlinearity. The characteristics of the RF MEMS-based variable attenuators reported by Khaira et al (2019) exhibit substantial dB-nonlinearity, which mainly stems from the highly nonlinear relationship between the attenuation and the moving electrode displacement. The main motivation of this study is to introduce dB-linear RF MEMS variable attenuators. The proposed devices utilize shaped-finger comb-drive actuators to improve dB-linearity.

Previously, we have reported a novel shaped-finger comb-drive design method for a variable capacitor (Hah 2022). Different from the other design methods where finger shapes were calculated from well-defined force profiles (Ye et al 1998; Jensen et al 2003; Lee et al 2008; Engelen et al 2010), the author's method calculates finger shapes analytically by solving an objective governing differential equation, which is set by the desired device performance outcome. Earlier, the method was used to design varactors with linear capacitance-voltage relationships. In this work, the design method is revisited in order to achieve a dB-linear variable attenuator. In addition, the design method is further improved by taking the spring nonlinearity into account. In the previous work (Hah 2022), the mechanical spring of the actuator was assumed as a linear one. This is a reasonable approximation for a small range of displacement. However, as the travel range increases, and hence, as the strain/stress experienced by the spring structure becomes higher, discrepancy between the actual spring behavior and the linear spring approximation widens. The modified design method that includes the spring nonlinearity is further described in Sect. 3. Section 2 will present the operation principle and the RF numerical simulation results of the variable attenuator. The dB-linearity performance of the proposed devices will be reported in Sect. 3.

## 2 Operation principle

Figure 1 illustrates a schematic diagram of the RF variable attenuator. The input signal is equally divided into two by the first hybrid coupler, and each of the divided signals passes through one of the MEMS parts. At this point, the MEMS parts control the transmission/reflection of the signals. The transmitted powers are combined by the second hybrid coupler, and then, sent to the output port. The reflected powers are combined by the first hybrid coupler, and then, sent to the 50-Ω matching load on the input side. The other output port of the second hybrid coupler is also terminated with a 50-Ω matching load to minimize reflection at that point. The purpose of employing hybrid couplers is to avoid backward transmission of the reflected signal to the input port. Each hybrid coupler adds 3 dB of insertion loss.

Some details of the MEMS parts are also illustrated in Fig. 1. The key component of the MEMS parts is a moving electrode that is connected to the electrical ground. The presence of this moving electrode creates disruption in the propagation of the RF signal through the CPWs, which results in reflection. One moving electrode is added on

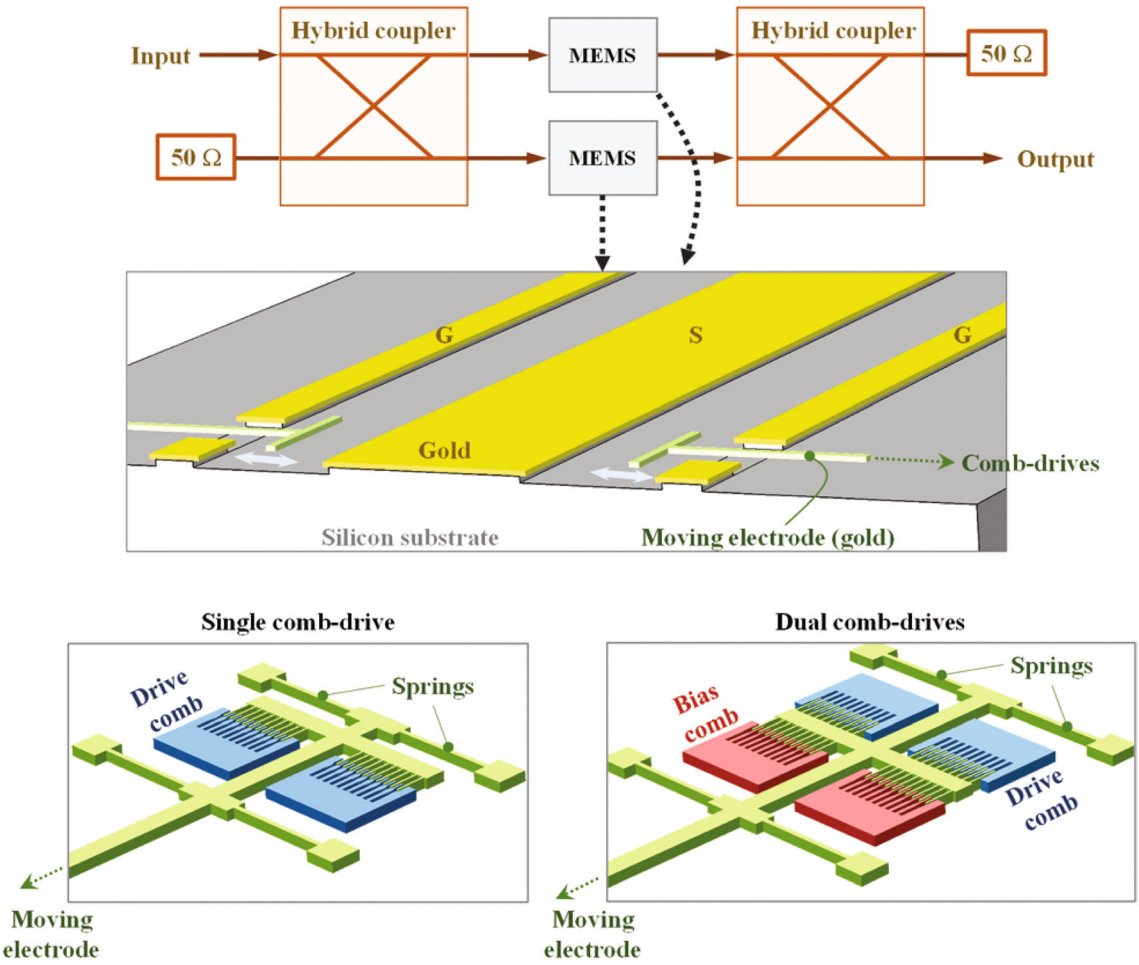


**Fig. 1** Schematic illustrations of an RF MEMS variable attenuator. (Top) RF circuit, (middle) MEMS part: CPW with moving electrodes, (bottom) comb-drive actuators: single and dual

each side of the signal line to double the effect. The locations of the moving electrodes are controlled by comb-drive actuators, to which they are attached. The levels of reflection ($S_{11}$) and the insertion loss ($S_{21}$) depend on the distance between the moving electrode and the signal line. Therefore, a close investigation is necessary to understand the relationship between this distance ($g_{me}$) and the insertion loss ($S_{21}$). Modelling the MEMS parts simply as variable capacitors turned out to be an oversimplification of what actually occurs. There are other effects that take place as well, such as change in inductive coupling. Consequently, in order to understand the effects of the moving electrodes more accurately, numerical simulation was carried out by using CST Studio Suite®.

Figure 2 summarizes the flow of the study. First, RF simulation is carried out to establish the relationships between the moving electrode distance ($g_{me}$) and the attenuation ($A = -S_{21}$) in the MEMS part. At the same time, structural mechanics simulation is conducted to obtain the relationship between the mechanical restoring force ($F_{mech}$) and the beam deformation ($x$). These two relationships are used to formulate the governing differential equation, which is numerically solved to calculate

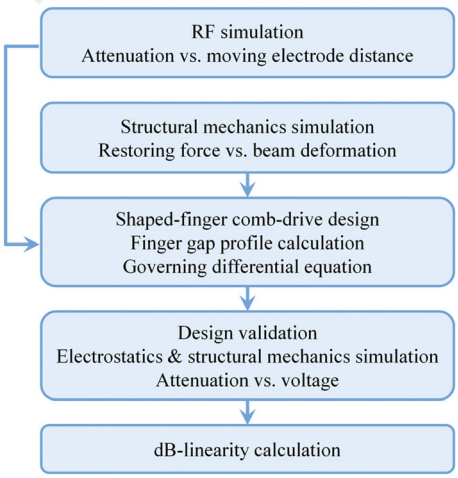


**Fig. 2** Flowchart of the study

the finger gap profile. The next step is the validation of the design. Electrostatics simulation is performed on the produced finger design, and its result is combined with the mechanics simulation result to generate the attenuation-voltage curve. Finally, the dB-linearity is calculated from the generated curve.

## 2.1 RF simulation

As the transmission line of the RF signal, Finite Ground CPW (FGCPW) was selected, which is most suitable for the proposed device configuration. In this work, silicon was chosen as the dielectric substrate and gold as all of the conductor parts. Air gap was considered under the moving electrodes. Also considered were the undercuts of the silicon substrate around the edges of the fixed structures, which are formed during the release step, i.e. substrate etching. The nominal geometrical dimensions of the key parts of the device are summarized in Table 1. The dimensions of the FGCPW were chosen to result in 50-Ω characteristic impedance.

Figures 3a and b show the simulation results of the return loss ($S_{11}$) and the insertion loss ($S_{21}$) of the MEMS variable attenuator between 15 GHz and 30 GHz, for various gaps ($g_{me}$) between the moving electrode and the signal line. The simulation did not include the hybrid couplers. A general trend is observed; the insertion loss increases as frequency increases, which can be understood as the stronger capacitive/inductive coupling occurring at higher frequency. The relationships between the return/insertion losses and $g_{me}$ at a specific frequency (20 GHz) are depicted in Fig. 3c and 3d. The $S_{21}$-$g_{me}$ relationship is significantly nonlinear as expected. Moreover, as the moving electrode approaches very close to the signal line, the trend is reversed, and the insertion loss starts to decrease. The reason for this behavior is understood as the combined effects of capacitive and inductive coupling. This explanation is further supported by Figs. 3e and f, which show that the moving electrode gap ($g_{me}$) for the maximum insertion loss depends on the frequency.

From the RF characteristics obtained for the device with the dimensions given in Table 1, the region of interest was defined as between 3.9 μm ($g_{me1}$) and 13.9 μm ($g_{me2}$) as indicated in Fig. 3d, considering several factors, such as attenuation dynamic range, operation voltage, and dB-linearity. With this region of interest definition, the displacement range ($x_{dr}$) becomes 10 μm (= $g_{me2} - g_{me1}$), and the attenuation range is between 1.9 dB and 19.7 dB, resulting in the dynamic range of 17.8 dB. It will be ideal to model the relationship between $S_{21}$ and $g_{me}$ analytically for an expedited design flow. Since it was difficult to find such an analytical relationship, however, it was fitted to an exponential function within the region of interest, as follows.

$$S_{21}(dB) = 0.82 - 108.37 \exp\left(-\frac{g_{me}}{1.94}\right) - 7.9 \exp\left(-\frac{g_{me}}{13.12}\right) \quad (1)$$

where $g_{me}$ is in μm. (1) is used in the governing differential equation in the later process. Figures 3c and d also include the case of a longer (500 μm) moving electrode. Compared to the case of a shorter (250 μm) $L_{me}$, the insertion loss starts to increase at a wider gap, as can be expected due to a stronger capacitive/inductive coupling effect. However, it can also be learned that with a longer moving electrode, the range of the electrode displacement required for the same dynamic attenuation range ($x_{dr}$) becomes wider to be 19.4 μm, which is disadvantageous. On the other hand, if $L_{me}$ is too short, its coupling effect becomes insufficient. Based on these findings, 250 μm was selected as an optimum value for $L_{me}$. In the following section, the details of the shaped-finger comb-drive actuator design method for high dB-linearity will be provided.

**Table 1** Nominal geometrical dimensions of the device considered in the study

| Description | Value | Description | Value |
|---|---|---|---|
| Signal line width ($W_S$) | 400 μm | Ground line width ($W_G$) | 100 μm |
| Electrode/[1]beam/finger thick. ($T$) | 10 μm | Moving ground width ($W_{me}$) | 20 μm |
| Signal-to-ground gap ($G$) | 250 μm | Moving ground length ($L_{me}$) | 250 μm |
| Substrate thickness ($T_{sub}$) | 500 μm | Moving ground gap 1 ($g_{me1}$) | 3.9 μm |
| [1]Beam length ($L_B$) | 2000 μm | Moving ground gap 2 ($g_{me2}$) | 13.9 μm |
| [1]Beam width ($W_B$) | 5 μm | No. comb fingers ($N_f$) | 200 |
| Finger gap @ far end ($d_f$) | [2]1 or 2 μm | Moving finger width ($W_{mf}$) | 2 μm |
| Finger gap @ near end ($d_n$) | [2]1 or 2 μm | Displacement range ($x_{dr}$) | 10 μm |

[1]Clamped-clamped beam as a spring

[2]Depending on the comb type (single or dual)

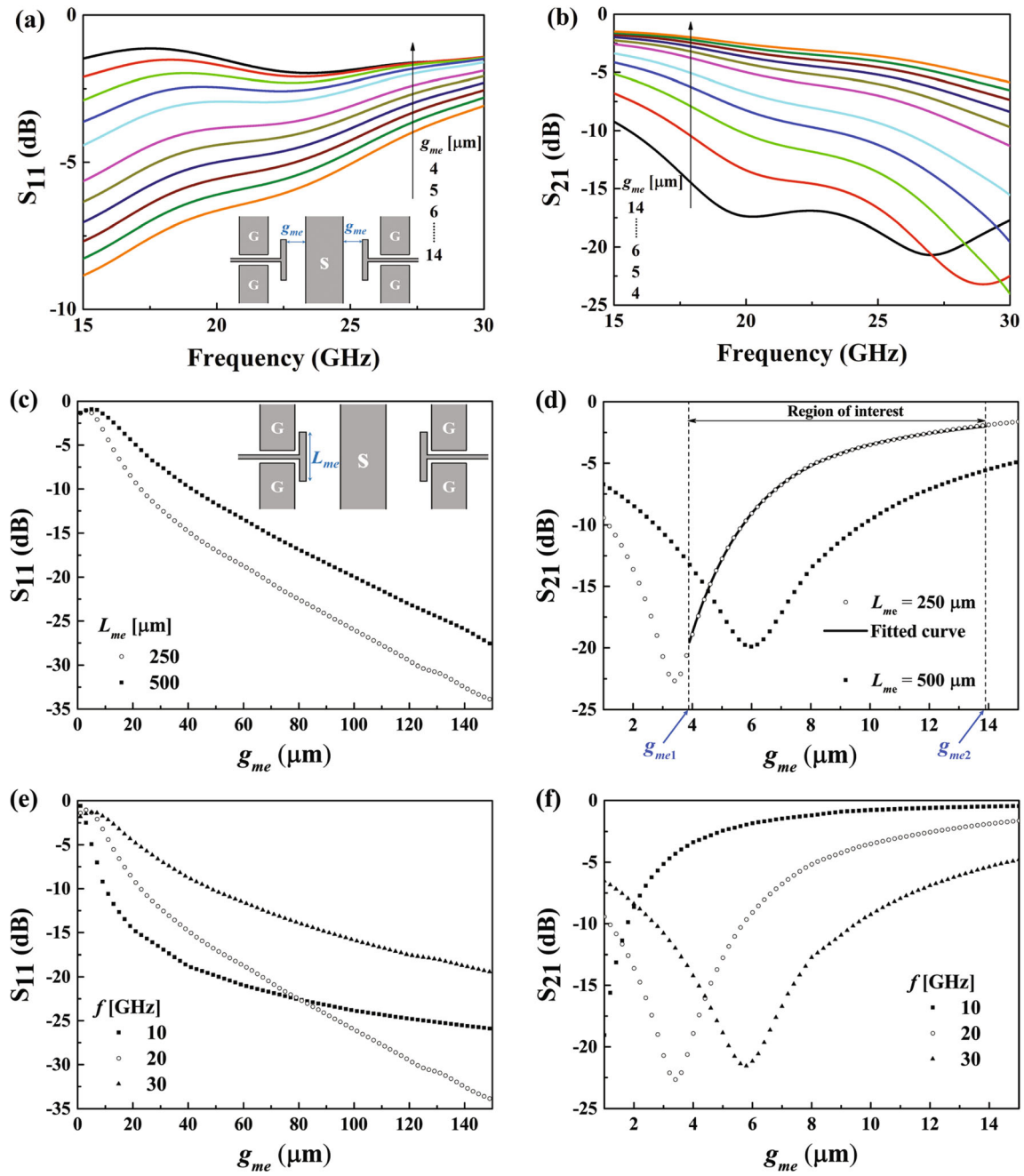


**Fig. 3** RF simulation results of MEMS variable attenuators. **a** $S_{11}$ vs. frequency for various moving electrode gaps, $g_{me}$. (Inset) top view of MEMS part. **b** $S_{21}$ vs. frequency for various $g_{me}$. **c** $S_{11}$ and **d** $S_{21}$ as a function of $g_{me}$ at 20 GHz. A fitting curve is included in **d** when $L_{me}$ is 250 μm. **e** $S_{11}$ and **f** $S_{21}$ as a function of $g_{me}$ at various frequencies

## 3 MEMS design and results

As illustrated in Fig. 1, the springs of the device have the fixed-guided boundary condition. Since the deformation of the non-spring structures is negligible, the springs can be modeled as clamped-clamped beams when put together. The large-deformation nonlinearity of a clamped-clamped beam due to mid-plane stretching is well documented in (Casals-Terre et al. 2008; Hajati and Kim 2011; Rezaei et al. 2012), which can be expressed as follows, with the linear term ($k_1$) and the cubic term ($k_3$).

$$F_{mech}(x) = k_1 x + k_3 x^3 \tag{2}$$

where,

$$k_1 = \frac{\pi^4 E T W_B^3}{6 L_B^3}$$

$$k_3 = \frac{\pi^4 E T W_B}{8 L_B^3}$$

and $F_{mech}$, $x$, and $E$ are mechanical restoring force, displacement of the beam center, and Young's modulus (for gold, 70 GPa), respectively. The definitions of other symbols can be found in Table 1. Figure 4a shows the calculated $F_{mech}$ (red curve) by using (2) with the dimensions given in Table 1. In order to obtain more accurate results, structural mechanics simulation was carried out by using COMSOL Multiphysics® (version 5.2), as plotted in Fig. 4a (squares). The simulation results are similar to the analytical ones. However, due to the slight discrepancy between the two results, the simulation result was fitted with a third-degree polynomial as written inside Fig. 4a, and used in the governing differential equation.

A more straightforward design is to employ a single comb-drive actuator (see Fig. 1), in which the moving electrode approaches the signal line as the moving fingers are more deeply engaged with the fixed fingers when a voltage is applied between them. However, as will be explained in the following subsection, it turns out that the high dB-linearity can be obtained only at the cost of a potential instability issue in the case of a single comb-drive device. Therefore, another type of device, i.e. with the dual comb-drives, was examined in this study as well, which will be presented in Sect. 3.2.

### 3.1 Single comb design

Figure 4c shows a unit of the comb-drive, i.e. a half of the moving finger and a half of the fixed finger. The three-dimensional (3-D) capacitance of the unit, $C_{DRIVE}$ can be approximated as an integral of the unit 2-D cross-sectional capacitance, $C_{drive}$ along the finger length direction, $u$.

$$C_{DRIVE}(x) = \int_{-l_{ol}}^{x} C_{drive}(u)\, du \tag{3}$$

where $l_{ol}$ is the as-fabricated overlap length between the fingers. $C_{drive}$ is calculated by the conformal mapping method (Johnson and Warne 1995; Hah 2022). The balance equation between the electrostatic force, $F_{elec}$ and the mechanical restoring force can be written as,

$$F_{elec}(x) = 2N_f \times \frac{1}{2}\frac{dC_{DRIVE}}{dx} V^2 = N_f C_{drive}(x) V^2 = F_{mech}(x) \tag{4}$$

where $V$ is the voltage applied to the comb-drive, and $F_{mech}$ is given in Fig. 4a. The objective of the design, i.e. dB-linearity, can be expressed as,

$$\frac{dS_{21}}{dV} = c_{dblin} \tag{5}$$

where $c_{dblin}$ is a linearity coefficient, defined by the maximum and the minimum values of $S_{21}$ and $V$ within the region of interest. By taking the first derivative of (4), and by combining it with (1), (4) and (5), one can obtain the following governing differential equation.

$$\frac{dC_{drive}}{dx} = \left(\frac{1}{F_{mech}}\frac{dF_{mech}}{dx} - \frac{2}{c_{dblin} V}\frac{dS_{21}}{dx}\right) C_{drive} \tag{6}$$

(6) was solved numerically by using Euler's method in MATLAB® to produce $C_{drive}$ as a function of $x$. Then, $d_{drive}(x)$, the finger gap profile, in other words, the shape of the finger, was found from $C_{drive}(x)$.

Figure 4b presents the calculated $d_{drive}$ for various design parameter values, $x_i$ and $x_{nex}$. $x_i$ (see Fig. 4d) is a parameter that is unavoidable in the single-comb devices because (6) does not have a solution at $x = 0$. In other words, $x_i$ is a length of an excluded zone, which starts from $x = 0$. At low voltage, i.e. between $x = 0$ and $x = x_i$, the RF performance of the device is to be excluded and ignored. $x_{nex}$, a near-side extension (see Fig. 4d), is another parameter that is introduced to improve the dB-linearity further. The idea is to design the device with an overshoot in terms of the dynamic range so that there can be an advantage in the dB-linearity when examined only within the region of interest ($x_{dr}$). The relationship between $x$ and $g_{me}$ is set as

$$g_{me} = g_{me2} - x + x_i. \tag{7}$$

For example, when $x = x_i$, $g_{me}$ becomes $g_{me2}$ ($S_{21} = -1.9$ dB). When $x = x_i + x_{dr}$, $g_{me}$ becomes $g_{me1}$ ($S_{21} = -19.7$ dB). For $x > x_i + x_{dr}$, $g_{me}$ is less than $g_{me1}$, but this part is not of interest. Since the extended region is near the signal line, it is called a near-side extension. For the dual-comb devices, extensions are considered on both sides, i.e. near and far. For a single-comb design, $d_n$, the finger gap at the near end (@ $x = x_i + x_{dr} + x_{nex}$) was set as 1 μm while $d_f$, the finger gap at the far end (@ $x = x_i$) was set as 2 μm.

The finger gap profiles presented in Fig. 4b (see also Fig. 4d for some examples of the finger shapes) do not seem to change much for different design parameters. With a close look, however, several observations can be made. In all cases, there are regions where the finger gap becomes smaller than $d_n$, 1 μm. This narrow finger gap does not incur a serious fabrication problem because the moving fingers are not deeply engaged with the fixed fingers as-fabricated as can be seen from Fig. 4d. However, such a small finger gap can lead to lateral instability and/or structure rotation when deeply engaged during actuation (Huang and Lu 2004; Borovic et al. 2006), and hence, is better to be avoided. Figure 4b shows that as $x_i$ increases,

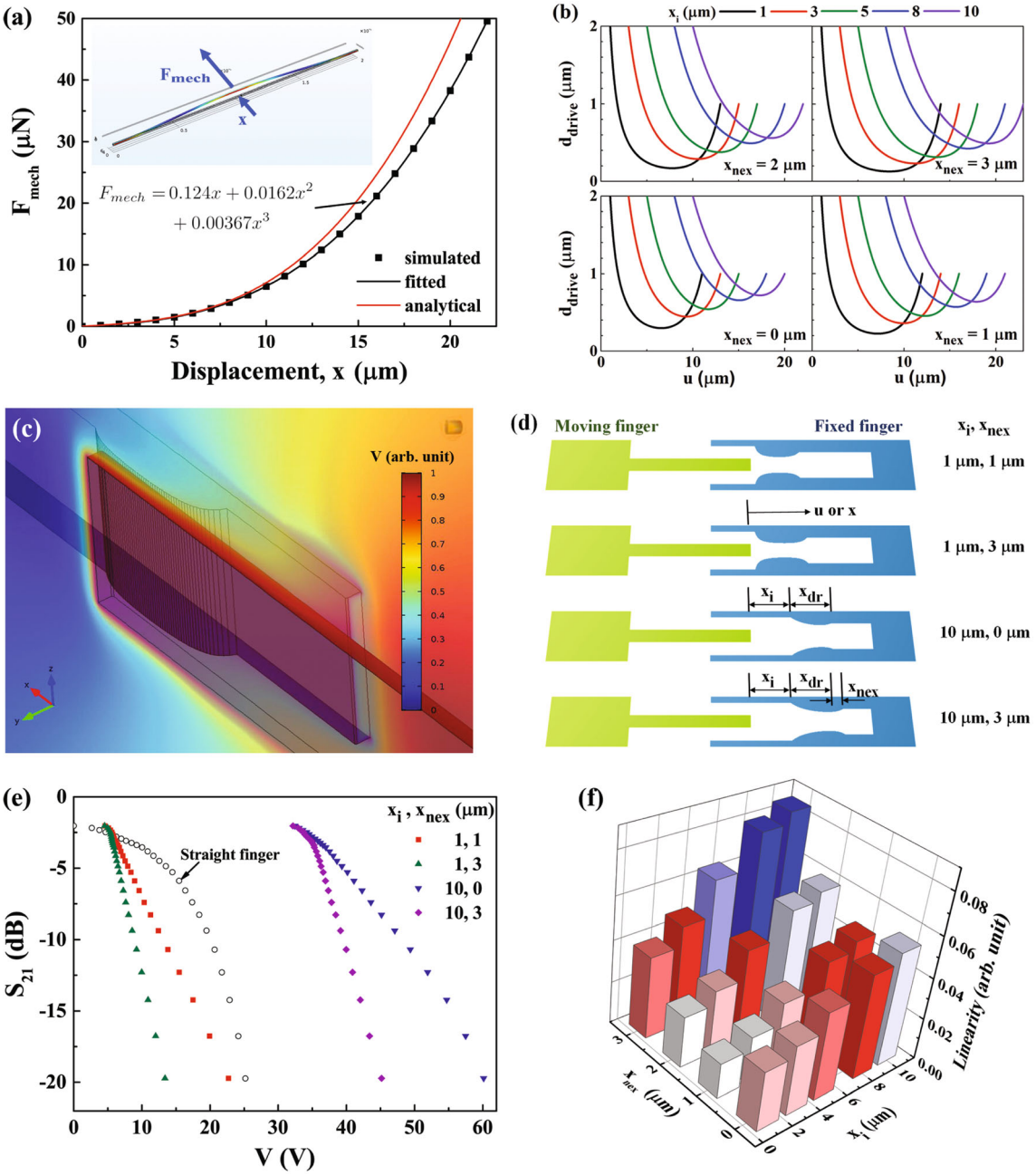


**Fig. 4** Simulation results of RF variable attenuators with single comb-drive actuators. **a** Mechanical force vs. center displacement of a clamped-clamped beam by simulation (square), by fitting (black line), and by analytical calculation (red line). (Inset) Snapshot from structural mechanics simulation, with color map indicating stress distribution. **b** Profiles of shaped finger gaps for various excluded zone widths, $x_i$ and near-side extensions, $x_{nex}$. **c** Snapshot from electrostatics simulation, with color map indicating electric potential. **d** Examples of finger shapes. **e** $S_{21}$ vs. applied voltage ($V$) for exemplary design parameter combinations. Result with a conventional straight-finger comb-drive is plotted as well for comparison. Data are plotted for a fixed range, from $g_{me} = g_{me1}$ (3.9 μm, $A$ = 19.7 dB) to $g_{me} = g_{me2}$ (13.9 μm, $A$ = 1.9 dB). (f) Linearity for various $x_i$ and $x_{nex}$ values

the narrowest finger gap for a particular design becomes wider. Therefore, a high value of $x_i$ is favorable in this respect although it requires higher operation voltage. Another observation is that when $x_{nex}$ increases, the range of the narrow finger gap region also increases.

Once the shaped-finger designs were obtained, they were examined through finite-element analysis (FEA) simulation by using COMSOL Multiphysics® for validation. The coupling between structural mechanics and electrostatics was carried out externally due to limited computational power resources (a general-purpose

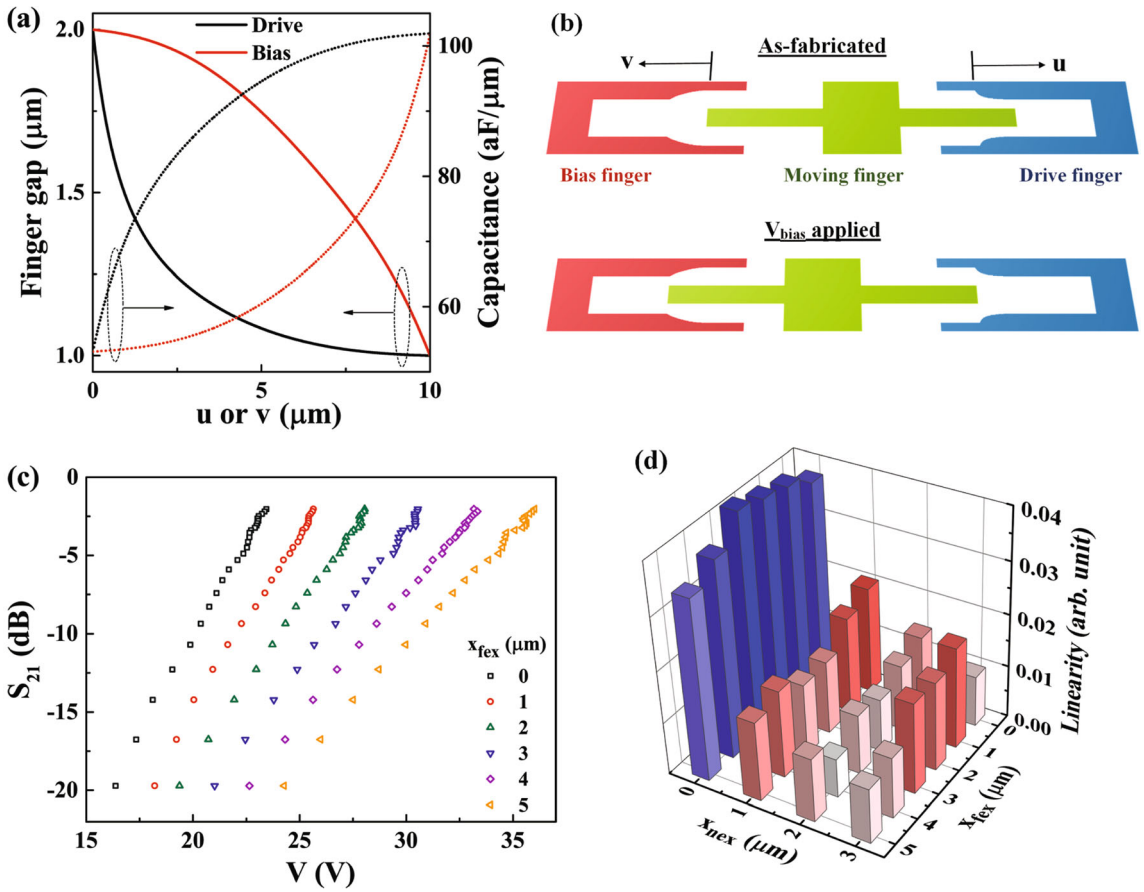


**Fig. 5** Simulation results of RF variable attenuators with dual comb-drive actuators. **a** Shaped-finger gap profiles, $d_{drive}(u)$ and $d_{bias}(v)$, and unit 2-D capacitance, $C_{drive}(u)$ and $C_{bias}(v)$. $x_{nex} = x_{fex} = 0$. **b** Examples of finger shapes, (top) as-fabricated, (bottom) when $V_{bias}$ is applied. **c** $S_{21}$ vs. $V$ for various far-side extension ($x_{fex}$) values when $x_{nex}$ = 2 μm. Data are plotted for a fixed range, from $g_{me} = g_{me1}$ ($A$ = 19.7 dB) to $g_{me} = g_{me2}$ ($A$ = 1.9 dB). **d** Linearity for various $x_{nex}$ and $x_{fex}$ values

computer). Figure 4c exhibits an example of electrostatics simulation results, showing electric potential distribution. The ultimate outcomes, $S_{21}$ versus $V$, for some exemplary cases are presented in Fig. 4e along with that of a device with conventional straight fingers (additional $S_{21}$-$V$ results are given in Online Resource 1). It should be noted that the graph only shows the data for the region of interest. For each group of the data, points are evenly distributed in terms of $x$. As expected, the shaped-finger devices exhibited improved dB-linearity in comparison to the conventional device. In general, the dB-linearity appeared to be better on the near side (high $V$) than the far side (low $V$).

For a quantitative comparison of dB-linearity, it was defined as the average distance of the normalized data points from the standard line, either $y = x$ or $y = 1 - x$, $x \in [0, 1]$, depending on the ascending or descending tendency of the data. The smaller this average distance is, the better the dB-linearity is. The linearity of the conventional device in Fig. 4e is calculated as 0.1969. The values of the linearity of the shaped-finger devices for various design parameters are plotted in Fig. 4f, which range from 0.0166 to 0.0858. When $x_{nex} = 0$, i.e. when the near-side extension is not utilized, the range of the linearity is from 0.0281 to 0.0549. The best overall linearity, 0.0166, was obtained with $x_i = x_{nex} = 1$ μm. This equals to an improvement of about a factor of twelve from the conventional device. This result, however, is not so welcoming because the design with $x_i = x_{nex} = 1$ μm requires the finger gaps as narrow as 0.2 μm while being operated. In the following subsection, device designs with dual-combs will be presented.

## 3.2 Dual comb design

The issue of undesirably narrow finger gaps in the case of single-comb devices can be addressed by adding a bias comb, which reverses the trend of the $S_{21} - V$ relationships and relaxes the nonlinearity to some degree (Hah 2017, 2020). As illustrated in Fig. 5b, the moving fingers are more engaged into the drive comb as-fabricated. First, a bias voltage ($V_{bias}$) is applied to the bias comb so that the moving fingers are drawn to it, and hence, more engaged with it. The bias comb is placed at the near side of the

FGCPW so that when $V$ (voltage on the drive comb) is zero, the variable attenuator is at the maximum attenuation. As $V$ increases, the moving fingers are drawn towards the drive comb, reducing the attenuation. The balance equation now becomes,

$$N_f\left[V_{bias}^2 C_{bias}(x) - V^2 C_{drive}(x_{max} - x)\right] = F_{mech}(x) \quad (8)$$

where $x_{max}$ is the maximum displacement range of the moving fingers, i.e. $x_{dr}$ plus extension lengths ($x_{nex}$, $x_{fex}$). The relationship between $C_{bias}$ and $C_{drive}$ is defined as,

$$C_{bias}(v) + C_{drive}(x_{max} - v) = C_{bias}(0) + C_{bias}(x_{max}). \quad (9)$$

The new governing differential equation becomes,

$$\frac{dC_{bias}}{dx} = \frac{2N_f V C_{drive}(x_{max} - x)\frac{dS_{21}}{dx} + c_{dblin}\frac{dF_{mech}}{dx}}{c_{dblin}N_f(V_{bias}^2 + V^2)}. \quad (10)$$

As can be understood from (10), the dual-comb design has a solution at $x = 0$ unlike the case of the single-comb design. Therefore, there is no need to consider an excluded zone ($x_i$) in the dual-comb device.

The rest of the design and validation processes are similar to those of the single-comb devices. First, (10) is numerically solved to find $d_{bias}(v)$, and then, $d_{drive}(u)$ is calculated by using (9). Figure 5a shows the calculated 2-D capacitances, $C_{drive}$ and $C_{bias}$, and the finger gap profiles, $d_{drive}$ and $d_{bias}$, when there is no extension. For a bias comb, $d_n$, the finger gap at the near end was set as 1 μm while $d_f$, the finger gap at the far end was set as 2 μm. For a drive comb, $d_n$ and $d_f$ were 2 μm and 1 μm, respectively. It can be observed that the finger gaps never become narrower than 1 μm, which is beneficial to mitigate the lateral instability problem. This is one of the merits of the dual-comb devices.

Once again, the designs were examined through FEA simulation. In the case of the dual-comb designs, the effects of the extension zones were examined on both sides, i.e. the near side ($x_{nex}$) and the far side ($x_{fex}$). Figure 5c presents the simulation results of $S_{21}$-$V$ for various values of $x_{fex}$ when $x_{nex}$ is 2 μm (additional $S_{21}$-$V$ results are given in Online Resource 1). It can be observed that when $x_{fex}$ is 4 μm, the $S_{21}$-$V$ characteristic curve looks the straightest. The linearity values were calculated for various extension lengths as plotted in Fig. 5d. The linearity turns out to be the worst when there is no extension on the near side, i.e. when $x_{nex}$ equals to 0. The best linearity, 0.0074 is obtained when $x_{nex}$ is 2 μm and $x_{fex}$ is 4 μm. This value is 26.6 times better than that of the conventional single-comb device, and 2.2 times better than the best linearity obtained from the shaped single-comb devices. It is also 2.8 times better than that of the dual-comb device with the conventional straight fingers.

## 4 Conclusion

Variable attenuators are key components in RF circuits and systems. In this work, RF MEMS variable attenuators with shaped-finger comb-drive actuators were proposed. Numerical simulation study has shown promising improvement in dB-linearity, which is attributed to novel finger shape designs. Two different types of actuators were examined, and the dual-comb type has shown better dB-linearity than the single-comb type. Further works include fabrication and characterization of the proposed devices.

**Acknowledgements** This work was partially supported by the Research Fund of Abdullah Gül University (FOA-2016-49).

## Declarations

**Conflict of interest** The author has no competing interest to declare that are relevant to the content of this article.

## References

Borovic B, Lewis F, Liu A et al (2006) The lateral instability problem in electrostatic comb drive actuators: modeling and feedback control. J Micro mech Microeng 16(7):1233. https://doi.org/10.1088/0960-1317/16/7/017

Casals-Terre J, Fargas-Marques A, Shkel AM (2008) Snap-action bistable micromechanisms actuated by nonlinear resonance. J microelectromech syst 17(5):1082–1093. https://doi.org/10.1109/JMEMS.2008.2003054

Chang S, Sivoththaman S (2006) A tunable rf mems inductor on silicon incorporating an amorphous silicon bimorph in a low-temperature process. IEEE Elect Device Lett 27(11):905–907. https://doi.org/10.1109/LED.2006.884712

Da Rezaei H, Kadkhodaei M, Nahvi H (2012) Analysis of nonlinear free vibration and damping of a clamped-clamped beam with embedded prestrained shape memory alloy wires. J Intel Mater Syst Struct 23(10):1107–1117. https://doi.org/10.1177/1045389X12441509

Destino G, Kursu O, Tammelin S, et al (2017) System analysis and design of mmw mobile backhaul transceiver at 28 ghz. 2017 European Conference on Networks and Communications (EuCNC)

Engelen JBC, Abelmann L, Elwenspoek MC (2010) Optimized comb-drive finger shape for shock-resistant actuation. J Micro mech Microeng 20(105):003. https://doi.org/10.1088/0960-1317/20/10/105003

Gao H, Wang W, Fan W et al (2021) Design and experimental validation of automated millimeter-wave phased array antenna-in-package (aip) experimental platform. IEEE Trans Instrument Meas 70:1–11. https://doi.org/10.1109/TIM.2020.3024428

Habbachi N, Besbes K (2022) Rf mems filter based on dual liquid variations. J Micromech Microeng 32(6):065002. https://doi.org/10.1088/1361-6439/ac6203

Hah D (2017) A design method of comb-drive actuators for linear tuning characteristics in mechanically tunable optical filters. Microsyst Technol 23:3835–3842. https://doi.org/10.1007/s00542-015-2736-8

Hah D (2020) Linear variable optical attenuators with shaped-finger comb-drive actuators. Appl Opt 59:277–284. https://doi.org/10.1364/AO.59.000277

Hah D (2022) Analytical design of mems variable capacitors based on shaped-finger comb-drives. Microsyst Technol 28(6):1423–1434. https://doi.org/10.1007/s00542-019-04362-x

Hajati A, Kim SG (2011) Ultra-wide bandwidth piezoelectric energy harvesting. Appl Phys Lett 99(8):083–105. https://doi.org/10.1063/1.3629551

Huang W, Lu G (2004) Analysis of lateral instability of in-plane comb drive mems actuators based on a two-dimensional model. Sens Actuat A: Phys 113(1):78–85. https://doi.org/10.1016/j.sna.2003.12.032

Huang YY, Woo W, Yoon Y et al (2011) Highly linear rf cmos variable attenuators with adaptive body biasing. IEEE J Solid-State Circuit 46(5):1023–1033. https://doi.org/10.1109/JSSC.2011.2117530

Iannacci J, Tagliapietra G (2022) Getting ready for beyond-5g, super-iot and 6g at hardware passive components level: a multi-state rf-mems monolithic step attenuator analyzed up to 60 ghz. Microsyst Technol 28:1235–1240. https://doi.org/10.1007/s00542-022-05285-w

Jensen B, Mutlu S, Miller S et al (2003) Shaped comb fingers for tailored electromechanical restoring force. J Microelectromech Syst 12(3):373–383. https://doi.org/10.1109/JMEMS.2003.809948

Johnson W, Warne L (1995) Electrophysics of micromechanical comb actuators. J Microelectromech Syst 4:49–59. https://doi.org/10.1109/84.365370

Khaira NK, Singh T, Mansour RR (2019) Monolithically integrated rf mems-based variable attenuator for millimeter-wave applications. IEEE Transact Microwave Theory Tech 67(8):3251–3259. https://doi.org/10.1109/TMTT.2019.2925798

Kolodziej KE, McMichael JG, Perry BT (2016) Multitap rf canceller for in-band full-duplex wireless communications. IEEE Transact Wireless Commun 15(6):4321–4334. https://doi.org/10.1109/TWC.2016.2539169

Kumar D, Siju V, Pathak SK (2019) Design of rf agc scheme for improving dynamic range of multichannel heterodyne ece radiometer in sst-1 tokamak. Fusion Eng Design 142:80–84. https://doi.org/10.1016/j.fusengdes.2016.05.007

Lee KB, Lin L, Cho YH (2008) A closed-form approach for frequency tunable comb resonators with curved finger contour. Sens Atuators A: Phys 141(2):523–529. https://doi.org/10.1016/j.sna.2007.10.004

Levinger R, Yishay RB, Katz O et al (2016) High-performance e-band transceiver chipset for point-to-point communication in sige bicmos technology. IEEE Trans Micro Theory Tech 64(4):1078–1087. https://doi.org/10.1109/TMTT.2016.2528981

Rezaei DA, Kadkhodaei M, Nahvi H (2012) Analysis of nonlinear free vibration and damping of a clamped-clamped beam with embedded prestrained shape memory alloy wires. J Intel Mater Syst Struct 23(10):1107–1117. https://doi.org/10.1177/1045389X12441509

Saleh H, Shojaeian M, Bajwa R et al (2022) Low actuation voltage cantilever-type rf-mems shunt switches for 5g applications. Microelect Reliab 136(114):645. https://doi.org/10.1016/j.microrel.2022.114645

Sharaf A, Nasr A, Elshurafa AM et al (2022) Design analysis and simulation of a digital rf mems varactor with high capacitive ratio. Microsys Technol 28:1831–1844. https://doi.org/10.1007/s00542-022-05318-45

Sravani KG, Guha K, Aditya M et al (2022) Design, simulation and analysis of uniform and non-uniform serpentine step structure rf mems switch. Microsys Technol 28:855–865. https://doi.org/10.1007/s00542-021-05216-1

Sun KO, Choi MK, van der Weide D (2005) A pin diode controlled variable attenuator using a 0-db branch-line coupler. IEEE Micro Wire Comp Lett 15(6):440–442. https://doi.org/10.1109/LMWC.2005.850568

Ture Savadkoohi P, Margesin B (2022) Tuneable rf mems capacitors based on electrostatically induced torsion. Analog Integr Cir Sig Proc 110:431–441. https://doi.org/10.1007/s10470-021-01948-2

Wang K, Wang Z, Wang G et al (2017) Design of a low-insertion-phase-shift mmic attenuator integrated with a serial-to-parallel converter. IEICE Electron Exp 14(20):20170924. https://doi.org/10.1587/elex.14.20170924

Workie TB, Wu Z, Tang P et al (2022) Figure of merit enhancement of laterally vibrating rf-mems resonators via energy-preserving addendum frame. Micromach. https://doi.org/10.3390/mi13010105

Ye W, Mukherjee S, MacDonald N (1998) Optimal shape design of an electrostatic comb drive in microelectromechanical systems. J Microelectromech Syst 7(1):16–26. https://doi.org/10.1109/84.661380

Zhao D, Gu P, Zhong J et al (2021) Millimeter-wave integrated phased arrays. IEEE Transact Circuit Syst I: Reg Pap 68(10):3977–3990. https://doi.org/10.1109/TCSI.2021.3093093